JGR Oceans

RESEARCH ARTICLE
10.1029/2025JC023026

Energetics of the Upper-Ocean Under Sea Ice: Frictional Dissipation Versus Baroclinic Production

Mukund Gupta[1], **Andrew F. Thompson**[2], **and Patrice Klein**[2,3]

[1]Department of Geoscience and Remote Sensing, Delft University of Technology, Delft, The Netherlands, [2]Environmental Science and Engineering, California Institute of Technology, Pasadena, CA, USA, [3]LMD/IPSL, CNRS, Ecole Normale Supérieure, Polytechnique, PSL Research University, Paris, France

Key Points:

- In polar oceans, Ekman motions from sea ice—eddy interactions produce baroclinic energy that partially compensates frictional energy loss in the mixed layer
- At the surface, sea ice melt increases energy production at low and moderate ice concentrations (<80%) but reduces energy production at higher ice concentrations
- The discrete nature of sea ice floes modulates (sub-)mesoscale processes, sea ice motions, and melt rates

Correspondence to:

M. Gupta,
Mukund.Gupta@tudelft.nl

Citation:

Gupta, M., Thompson, A. F., & Klein, P. (2026). Energetics of the upper-ocean under sea ice: Frictional dissipation versus baroclinic production. *Journal of Geophysical Research: Oceans*, *131*, e2025JC023026. https://doi.org/10.1029/2025JC023026

Received 17 JUN 2025
Accepted 31 JAN 2026

Author Contributions:

Conceptualization: Mukund Gupta, Andrew F. Thompson
Formal analysis: Mukund Gupta, Andrew F. Thompson, Patrice Klein
Funding acquisition: Andrew F. Thompson
Methodology: Mukund Gupta
Project administration: Andrew F. Thompson
Software: Mukund Gupta
Visualization: Mukund Gupta
Writing – original draft: Mukund Gupta
Writing – review & editing: Mukund Gupta, Andrew F. Thompson, Patrice Klein

Abstract In polar regions, the presence of sea ice is known to reduce the ocean's eddy kinetic energy (EKE) by enhancing frictional dissipation at the surface. Here, using a coupled ocean—sea ice model, we discuss a mechanism that can instead increase EKE generation under sea ice and, in our simulations, compensates surface dissipation by 69% to 30% for sea ice concentrations varying between 30% and 100%. Mesoscale Ekman pumping and suction due to the sea ice cover give rise to vertical buoyancy fluxes in the core of mesoscale eddies, leading to rectified baroclinic energy production below the mixed layer. Additionally, in the shallow surface layer (∼5 m), heterogeneous sea ice melt generates mixed layer eddies that enhance baroclinic production for conditions typical of the summer marginal ice zone (MIZ). EKE dissipation and production are both affected by the dynamics of the individual ice floes resolved in our model, which result in distinct patterns of sea ice aggregation around ocean eddies, a preference for anticyclonic floe rotation in the MIZ, and size-dependent melt. These results emphasize the tightly coupled nature of ocean—sea ice interactions, and the challenge in capturing them within coarse and continuum-based models.

Plain Language Summary Eddies are swirling features of various sizes that are ubiquitous in the ocean. At the poles, these features may be damped by the presence of sea ice, which is a layer of frozen sea water that can form on the ocean surface and provide frictional damping to the underlying currents. This work uses numerical simulations representing a patch of the polar ocean to explore how pieces of ice influence ocean eddies, particularly when the sea ice cover is not fully compacted. The simulations show that sea ice indeed damps surface eddies, but also enhances their production rate by generating fine-scale circulation patterns in the upper ocean. These physics are likely not well represented by traditional climate models, which may bias sea ice melt rates and other critical polar ocean processes. This motivates the development of better numerical schemes that can help coarse models capture the detailed mechanisms noted in the high-resolution simulations used in this work.

1. Introduction

Sea ice is an important mediator of the rapid changes occurring over the polar oceans. In the Arctic, the decline in the areal concentration of summer sea ice has led to an observed increase in the upper-ocean heat content, primarily due to the ice-albedo feedback allowing a greater fraction of solar radiation to be absorbed at the surface (Kashiwase et al., 2017; Perovich et al., 2007; Timmermans et al., 2018). Over both poles, sea ice also influences turbulent heat exchanges at the air-sea interface (Loose et al., 2024), carbon storage into the ocean (Stephens & Keeling, 2000), the formation of deep waters (Zhang et al., 2021; Zhou et al., 2023), basin-wide ocean circulation patterns (Ferrari et al., 2014; Meneghello et al., 2018), and marine ecology (Arrigo, 2014). These ice-ocean interactions are difficult to capture within global climate models because they are modulated by processes that are typically unresolved, notably at the ocean mesoscale and sub-mesoscale (Manucharyan & Thompson, 2022). Appropriately representing sea ice rheology and thermodynamics at these scales also remains a challenge, with implications for sea ice drift (Rampal et al., 2011; West et al., 2022), melt rates (Gupta & Thompson, 2022; Horvat et al., 2016) and freezing mechanisms (Martínez-Moreno et al., 2025). As sea ice continues to become younger, thinner and weaker (Comiso, 2012; Sumata et al., 2023), it is important to better understand the role of eddying ice-ocean interactions on regional and global climate, and assess how they may evolve in the coming years.

While observations of ocean eddies underneath sea ice remain sparse, measurements taken over the last few decades suggest that these turbulent features may have distinct characteristics compared to their counterparts at

lower latitudes. In the Arctic, data from Ice Tethered Profilers (ITPs) and moorings within the seasonally ice-covered ocean reveal eddies that tend to be intensified within the halocline, and have comparably small diameters (~1–15 km), owing in part to the reduced deformation radius at high latitudes (Cassianides et al., 2023; Manley & Hunkins, 1985; Zhao et al., 2014). A majority of these eddies are anticyclonic, though their polarity may differ regionally and with depth (Pnyushkov et al., 2018). In the Southern Ocean, instrumented seals and gliders reveal significant sub-mesocale activity in the seasonal ice zone (Kosty et al., 2025; Prend et al., 2025; Swart et al., 2020), while moorings suggest signs of mesoscale eddy-induced heat upwelling on the continental shelf (Martinson & McKee, 2012). The presence of consolidated sea ice has generally been associated with a decline in surface eddy kinetic energy (EKE) due to frictional dissipation (Ou & Gordon, 1986) and a reduction in the baroclinic instability potential (Meneghello et al., 2021). Sub-mesoscale activity under ice may be enhanced in the summer, due to greater momentum transfer by winds (Mensa & Timmermans, 2017) or in winter due to baroclinic instability generated by sea ice leads (Cohanim et al., 2021; Manucharyan & Thompson, 2022). These seasonal dynamics are distinct from energetics at lower latitudes, where surface sub-mesoscale eddies are typically enhanced during winter, driven by the deepening of the mixed layer (Callies et al., 2016).

Marginal ice zones (MIZs) are energetic regions within the polar seas (Padman, 1995) where sea ice is particularly susceptible to breakage and melt induced by ocean and atmospheric forcing. Over the last few decades, the Arctic MIZ has broadly shifted northward and expanded to comprise a higher proportion of the total sea ice pack (Cocetta et al., 2024; Rolph et al., 2020). In contrast to the consolidated ice cover, the momentum balance of sea ice within the MIZ is strongly affected by storms, waves, swells and eddying ocean currents, as well as the heterogeneous state of the pack (Brenner & Horvat, 2024; Dumont, 2022; Martínez-Moreno et al., 2025; Vichi, 2022). At the ice edge, freezing and melt can also generate horizontal buoyancy gradients, which induce baroclinic instability at meso to sub-mesoscales (Gupta & Thompson, 2022; Horvat et al., 2016). The resulting eddies promote the lateral transport of heat, salinity and sea ice (Gupta et al., 2024; Manucharyan & Thompson, 2017), and may allow vertical mixing across the base of the mixed layer (Cohanim et al., 2021; Lo Piccolo et al., 2024).

Within the MIZ, sea ice is often fractured into individual pieces, called floes, whose mean diameters range between several meters and tens of kilometers (Stern et al., 2018). The floe size distribution (FSD) tends to display self-similarity across scales, with distributions often described by piece-wise power-laws or log-normal profiles (Denton & Timmermans, 2022; Horvat et al., 2019; Mokus & Montiel, 2022; Toyota et al., 2006). The slope of the FSD evolves on a seasonal time scale, with a higher proportion of smaller floes during the summer, reflecting more broken sea ice compared to the winter (Gupta et al., 2025; Stern et al., 2018). The granularity of the pack may also affect the net drag coefficient between the sea ice, ocean and atmosphere, as floes tend to increase the overall roughness of the pack due to edge effects (Mchedlishvili et al., 2023). The size and shape distribution of floes may also impact the mechanical stresses that occurs via collisions (Herman, 2018), the momentum response to external forcing (Bateson et al., 2020), and the propagation of surface waves (Boutin et al., 2021). These dynamics help characterize the properties of the MIZ (Roach et al., 2024; Thomson, 2022), but are challenging to represent using continuum-based sea ice models.

The development of discrete element models (DEMs) of sea ice has allowed more faithful representation of MIZ processes (Åström et al., 2024; Herman, 2013), including the coupled interactions between ocean eddies and resolved ice floes (Gupta & Thompson, 2022). These models have shown that sub-mesoscale ice-ocean interactions can cause smaller floes to melt faster, disperse more easily in the open ocean, and dissipate more EKE (Brenner et al., 2023; Gupta et al., 2024; Moncada et al., 2025). Coupled eddy-floe interactions depend on the floe size relative to surface ocean features, as well as on the effect of sea ice friction and thermodynamics on upper-ocean stratification and baroclinicity. Recently, Brenner et al. (2023) used simulations of resolved sea ice floes driven by an (uncoupled) model of ocean sub-mesoscale turbulence to show that sea ice has the potential to damp surface ocean currents even at low sea ice concentrations (<80%). This result contrasts with continuum-based parameterizations of internal sea ice mechanics used in most climate models, which produce only a negligible amount of oceanic energy dissipation at these low concentrations (Shrestha & Manucharyan, 2022).

This study builds on the work of Brenner et al. (2023), and considers both energy dissipation and production under sea ice. We use a DEM composed of circular unbreakable floes, two-way coupled with a dynamic ocean, to quantify the EKE budget, floe motions, and melt as a function of sea ice concentration. We find a previously unrecognized mechanism of EKE production below sea ice, whereby frictional interactions between ocean eddies

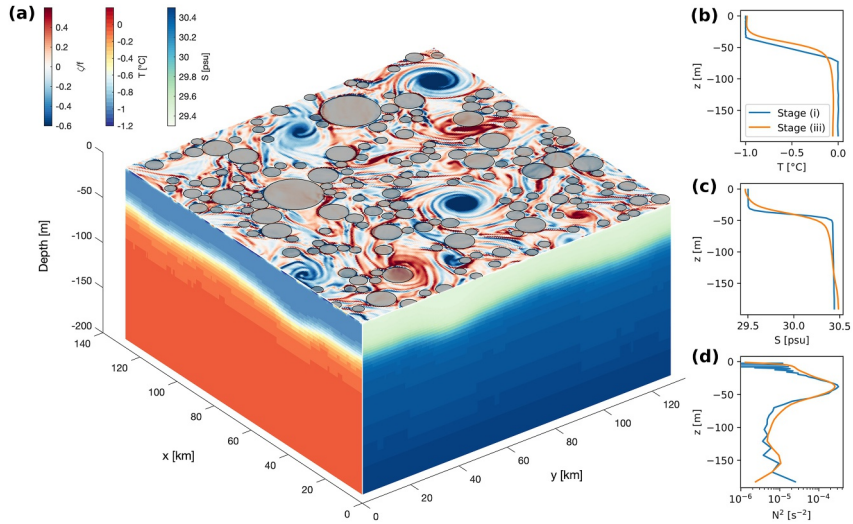

Figure 1. (a) Illustration of the coupled model of the upper ocean and circular sea ice floes at the end of the conc50 (50% sea ice concentration) simulation. The x-y slice shows a snapshot of the surface relative vorticity (ζ/f) along with the sea ice floes (gray circles). The x-z slice and y-z slices show snapshots of temperature and salinity, respectively. (b–d) Horizontally-averaged depth profiles at the start of stage (i) and stage (iii), respectively, for (b) temperature, (c) salinity and (d) vertical stratification N^2.

and sea ice generate anomalous Ekman vertical velocities, which drive EKE production underneath the mixed layer. This baroclinic production partially compensates dissipation from ice-ocean friction, and is therefore important to consider in parameterizations for ocean mixing under ice.

The manuscript is structured as follows: Section 2 presents the coupled model; Section 3 details the simulation results, including the effects of ice—eddy interactions on sea ice motions (Section 3.1), sea ice melt (Section 3.2), the ocean's EKE budget (Section 3.3), baroclinic EKE production in the upper-ocean (Section 3.4) and dynamics of the shallow melt layer (Section 3.5); Section 4 discusses the results; and Section 5 concludes.

2. Modeling Framework

2.1. Ocean Model

This study uses the "Oceananigans.jl" model (Ramadhan et al., 2020; Silvestri et al., 2025), which solves the 3-D Boussinesq equations for the ocean using a finite volume algorithm, closely based on the MITgcm (Marshall, Adcroft, et al., 1997; Marshall, Hill, et al., 1997). The model uses a pseudo-spectral pressure solver and parallelization over Graphical Processing Units (GPUs) in the Julia programming language. The domain consists of a box on an f-plane at 70°N latitude, with 500 m horizontal resolution and a stretched vertical grid resolution ranging from 1.3 m near the surface to 15 m at the bottom of the domain. The lateral and vertical extents of the domain are 128 km and 195 m, respectively (Figure 1). The boundary conditions are doubly periodic in the horizontal, rigid surface at the top, and no-flux at the bottom. The model uses a weighted essentially non-oscillatory (WENO) advection scheme with adaptive hyperviscosity (Silvestri et al., 2024), such that the numerical dissipation is implicit.

2.2. A Disk-Based Model of Sea-Ice Floes

The sea ice model simulates the motions and melt of sea ice floes (Gupta et al., 2024; Gupta & Thompson, 2022), where each floe is represented as a disk with constant radius in time. At every time step, the model evaluates the sea ice fraction over the oceanic grid by projecting the area of floes onto each cell that they intersect. Fluxes to the ocean are computed via a linearly weighted fraction of atmospheric and sea ice forcings for heat, salinity and momentum, based on the sea ice fraction at each grid cell. In the vertical, each floe is treated as a single-layer slab assumed to be at the freezing temperature (T_f), which is representative of summer-like conditions

Table 1
Prescribed Model Parameters

Quantity	Definition	Value	Units
α_o	Ocean albedo	0.4	–
α_i	Ice albedo	0.7	–
T_i	Ice temperature	−1.8	°C
S	Shortwave forcing	300	W m^{-2}
A	Outgoing heat flux constant	90	W m^{-2}
B	Outgoing heat flux coefficient	15	W m^{-2}K^{-1}
L_i	Latent heat of melting	3.34 ×10^5	J kg^{-1}
q_{io}	Ice-ocean heat exchange coefficient	100	W m^{-2} K^{-1}
U_a	Maximum air speed	4	m s^{-1}
L	Domain length	128	km
μ_f	Dynamic coefficient of friction	0.3	–
C_{oi}	Ice-ocean drag coefficient	0.0055	–
C_{ao}	Atmosphere/ocean drag coefficient	0.00125	–
C_{ai}	Atmosphere/ice drag coefficient	0.00125	–
ρ_a	Air density	1.25	kg m^{-3}
ρ_i	Ice density	1,000	kg m^{-3}
ρ_o	Reference ocean density	1,027	kg m^{-3}
f	Coriolis frequency	1.37 × 10^{-4}	s^{-1}
E	Ice elastic modulus	5.0 × 10^5	Pa
e_r	Ice coefficient of restitution	0.5	–
ν	Ice Poisson's ratio	0.33	–

(Thorndike, 1992). The sea ice thickness is uniform across a floe, but may vary in time due to surface and basal melt. The following thermodynamic equation is applied to each floe "k":

$$-\rho_i L_i \frac{dh_i^k}{dt} = S(1-\alpha_i) - (A + B\,T_i) + q_{io}\frac{\sum_g (T_o^g - T_i) A^g f^g}{\sum_g A^g f^g}, \quad (1)$$

where h_i^k is the floe thickness, A^g is the area of a grid cell "g" that intersects with this floe, f^g is the ice fraction of floe "k" within this grid cell, and T_o^g is the ocean temperature at the topmost model layer (Δz = 1.3 m). All other parameters are constants and described in Table 1. Melting of ice produces a fresh water forcing that is distributed uniformly in the horizontal under the floe, and the ice is assumed to be entirely fresh.

The translational and rotational motions of floes are described by the following equations, respectively:

$$m_i^k \frac{d\boldsymbol{u_i}^k}{dt} = \sum_g \left(\boldsymbol{\tau_{io}}^{k,g} + \boldsymbol{\tau_{ia}}^{k,g}\right) A^g f^g + \sum_{l\neq k} \boldsymbol{F}^{k,l} + m_i^k f \hat{\boldsymbol{k}} \times \boldsymbol{u}_i^k, \quad (2)$$

and

$$I_i^k \frac{d\Omega_i^k}{dt} = \sum_g \boldsymbol{r}^{k,g} \times \left(\boldsymbol{\tau_{io}}^{k,g} + \boldsymbol{\tau_{ia}}^{k,g}\right) A^g f^g + \sum_{l\neq k} \boldsymbol{R}^{k,l} \times \boldsymbol{F}^{k,l}, \quad (3)$$

where m_i^k is the mass of the floe, $\boldsymbol{u_i}^k$ is the floe velocity, $\boldsymbol{F}^{k,l}$ is the collision force exerted by floe "l" on floe "k," f is the Coriolis parameter, I_i^k is the floe's principal moment of inertia, Ω_i^k is the floe rotation rate, $\boldsymbol{r}^{k,g}$ is the vector directed from the floe center to the center of a grid cell "g" that intersect with the floe, and $\boldsymbol{R}^{k,l}$ is the vector directed from the floe center to the collision location. Equation 2 includes ocean and atmospheric stresses, collisions between floes, and the Coriolis force. Sea ice motion due to floes sliding along sea surface height anomalies is ignored in this model. The dynamical stresses from ocean to floe $\left(\boldsymbol{\tau_{io}}^{k,g}\right)$, atmosphere to floe $\left(\boldsymbol{\tau_{ia}}^{k,g}\right)$ and atmosphere to ocean $(\boldsymbol{\tau_{oa}}^{g})$ are parameterized as follows:

$$\boldsymbol{\tau_{io}}^{k,g} = \rho_o C_{oi}\left(\boldsymbol{u_o}^g - \boldsymbol{u_i}^k\right)\left|\boldsymbol{u_o}^g - \boldsymbol{u_i}^k\right|, \quad (4)$$

$$\boldsymbol{\tau_{ia}}^{k,g} = \rho_a C_{ai}\left(\boldsymbol{u_a}^g - \boldsymbol{u_i}^k\right)\left|\boldsymbol{u_a}^g - \boldsymbol{u_i}^k\right| \quad (5)$$

and

$$\boldsymbol{\tau_{oa}}^{g} = \rho_a C_{ao}(\boldsymbol{u_a}^g - \boldsymbol{u_o}^g)|\boldsymbol{u_a}^g - \boldsymbol{u_o}^g|, \quad (6)$$

where $\boldsymbol{u_o}^g$ and $\boldsymbol{u_a}^g$ are the ocean and atmospheric velocities, respectively. Collisions between floes are frictional and inelastic, and imply loss of both translational and rotational momentum according to Herman (2016). The relevant constants applied to the model are summarized in Table 1 and the starting sea ice thickness is 1 m for all floes. Ridging, rafting, welding, freezing and snow processes are not considered here.

2.3. Initial Conditions

The simulations are configured in three stages: (i) establishment of an eddying field in the ocean using spatially varying winds, (ii) relaxation to a quasi-steady state by turning off the wind forcing, and (iii) addition of sea ice floes and quantification of the coupled ice-ocean interactions. The first stage starts with a quiescent ocean, no sea

ice floes, and prescribed vertical profiles of temperature and salinity (Figure 1). These profiles define a cold and fresh layer in the top ∼30 m of the domain, that overlay warm and salty waters at the bottom. The mixed layer depth, defined by a potential density difference $\Delta\sigma_0 = 0.05$ kg m^{-3}, is 29 m at the start of stage (i) and 20 m at the start of stage (iii). Consistent with mooring observations in the Canada basin (Meneghello et al., 2021), the stratification profile (Figure 1), contains a peak at 41 m and another weaker peak at 162 m, which delimit the base of a characteristic "upper layer" and "halocline," respectively. As discussed in Section 3.5, sea ice melt during stage (iii) produces an additional "shallow melt layer" (∼top 5 m), characterized by a large stratification peak at its base that tends to isolate dynamics in this shallow layer.

The Rossby radius of deformation can be estimated as follows:

$$R_d = \frac{1}{f}\int N dz, \tag{7}$$

where N^2 is the buoyancy frequency and the integral is carried over the full depth of the domain. At the start of stage (i), R_d is 7.1 km and does not vary substantially in subsequent stages.

During stage (a), a steady wind velocity $\boldsymbol{u_a} = (u_a, v_a)$ is imposed on the ocean surface for 20 days:

$$\begin{cases} u_a = U_a \sum_{i=1}^{3} \sin\left(\frac{2\pi i x}{L} + \phi_{1,i}\right) \cos\left(\frac{2\pi i y}{L} + \phi_{2,i}\right), \\ v_a = U_a \sum_{i=1}^{3} -\cos\left(\frac{2\pi i x}{L} + \phi_{1,i}\right) \sin\left(\frac{2\pi i y}{L} + \phi_{2,i}\right), \end{cases} \tag{8}$$

where U_a is a prescribed maximum air speed, L is the domain length, and $\phi_{1,i}$ and $\phi_{2,i}$ are phases generated by random numbers. As in Brannigan et al. (2015), we only include the first three sinusoidal harmonics of the domain with the aim of generating mesoscale variability in the ocean. This wind forcing has zero mean when averaging in the zonal and meridional directions. In stage (ii), the wind forcing is turned off by setting $C_{ai} = 0$ and $C_{ao} = 0$, which allows the eddying field to equilibrate to a quasi-steady state. After 40 days without winds, the domain-mean EKE and the mean vertical profiles of temperature and salinity do not display any notable trend (not shown). In stage (iii), sea ice floes are distributed over the domain and the wind stress is kept turned off. The floes are initially stationaryand are subsequently accelerated by the eddying ocean currents. The characteristic time scale for a given sea ice floe to attain the mean surface velocity under ice for our model parameters is approximately 1 hr (Gupta & Thompson, 2022). However, there is always a finite, local ice-ocean velocity difference, since floes are constrained to move as solid bodies (unlike ocean eddies), and collisions can disrupt any established equilibrium. The ice-ocean velocity differences generate a net drag force on the ocean, causing a continuous decline in the ocean's kinetic energy content during stage (iii), which lasts 12 days. Most of our analysis pertains to this stage, and unless specified, the diagnosed quantities are averaged over the last 10 days.

Several sea ice concentrations are considered for stage (iii) of the numerical experiments, namely 10%, 20%, 30%, 40%, 55%, 64%, 72%, 80%, 85% and 100% (conc10, conc20, etc.), with the corresponding FSD shown in Figure 2. Floes are constrained to be of the following radii: 1, 2, 3, 5, 10, and 20 km. We attempt to maintain a relatively consistent FSD slope between experiments, but this is difficult due to packing constraints with circular floes, leading to lower α values at higher concentrations. Additionally, limits on the minimum floe size imposed by numerical stability prevents us from considering simulations with resolved floes that have a concentration higher than 85%. The simulation with 100% sea ice concentration does not include individual floes, but assumes that the ocean is completely covered by sea ice with zero drift velocity ($\boldsymbol{u_i} = 0$).

3. Results

3.1. Sea Ice Floe Motions

We first study the motions of sea ice floes by probing their spatial organization with respect to ocean eddies in three characteristic simulations: conc30, conc55, and conc80 (Figure 3). For conc30, floes are largely in free drift, with rotations that are both cyclonic and anticyclonic. The floes mostly coalesce in the periphery of mesoscale

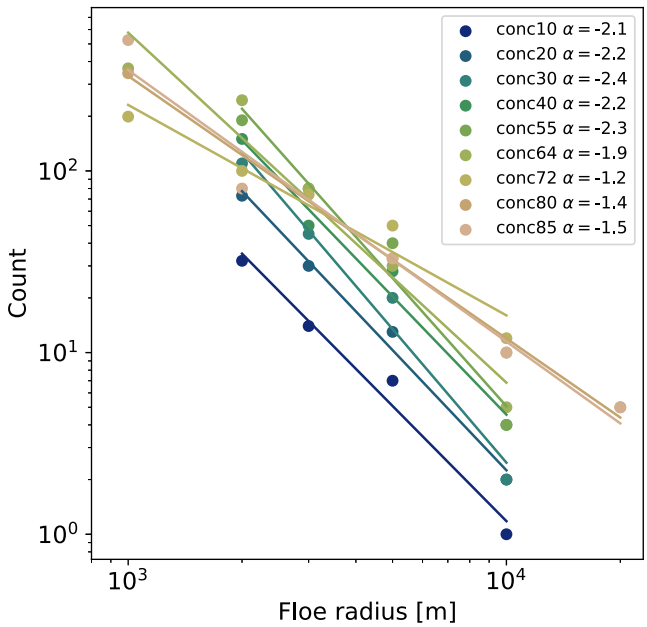

Figure 2. Imposed floe size distribution (FSD) for the numerical experiments considered in this study. Each experiment has a different sea ice concentration, and the the linear slope of the corresponding FSD (α) is displayed in the caption.

eddies, consistent with the dispersion of particles at the surface of the ocean by the large-scale strain field (Maalouly et al., 2023) and the expulsion of floes out of high-vorticity regions due to radial imbalance (Gupta et al., 2024; Zhang et al., 2015). The clustering of floes around mesoscale oceanic eddies becomes most apparent when visualizing the ocean's geostrophic sea surface height η_g, obtained by inverting the following expression for geostrophic balance:

$$\nabla^2 \eta_g = \frac{f\zeta_d}{g}, \tag{9}$$

where ζ_d is the depth-averaged relative vorticity. Cyclonic eddies have a depressed η_g, while anticyclonic eddies have an elevated η_g. For conc55, floes also tend to aggregate outside mesoscale eddies, but due to the higher sea ice concentration, some ice is pushed toward eddy cores via floe-floe collisions. Smaller floes can exit the center of eddies more easily than larger floes, whose size is comparable to mesoscale eddies. When the sea ice concentration is higher (conc80), the floes are tightly packed together, such that their motions are strongly constrained by collisions with neighboring floes.

The spatial distribution of floes and their interactions with underlying eddies affect their mean rotation rates and floe speeds (Figure 4). The rotation rate tends to decreases with floe size, as larger floes feel the influence of more collisions and eddying features, whose induced torques can partially cancel each other. Some simulations exhibit a slight increase in rotation rate for large floe sizes (e.g., conc64 and conc72), which is likely due to episodic collisions imparting significant torque on floes. On the other hand, the relationship between floe speed and floe radius is less consistent across simulations. At low sea ice concentrations (conc10 to conc30), the floe speed does not vary strongly with floe size. The floes

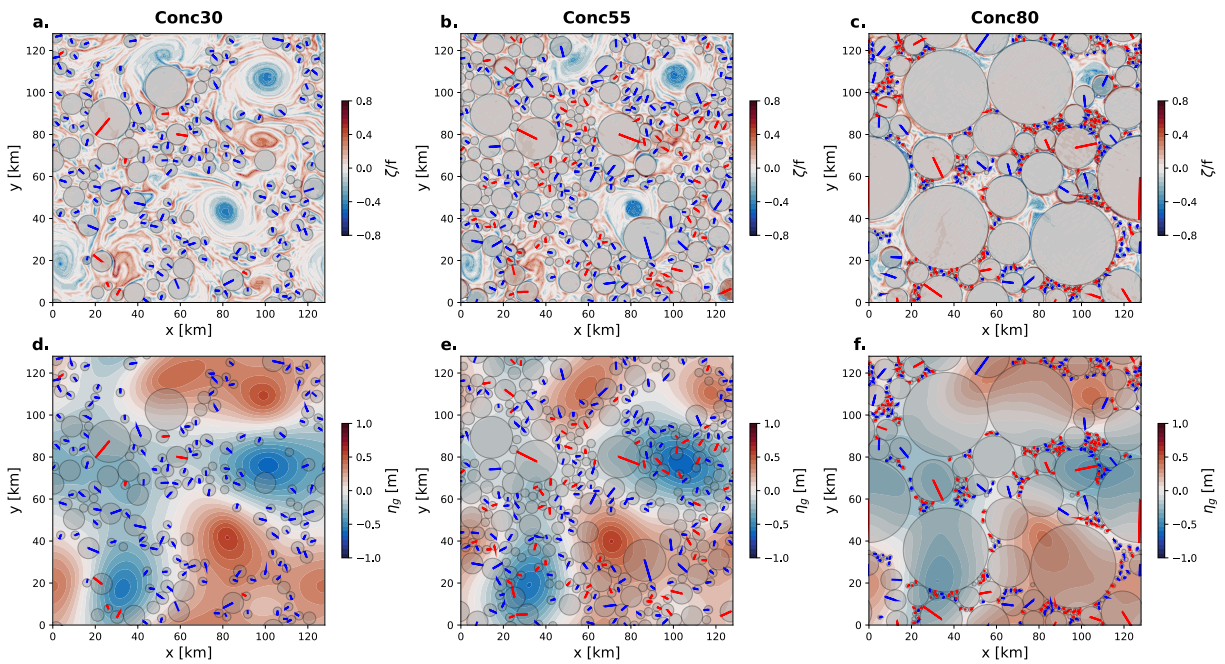

Figure 3. Surface snapshots of (top) surface relative vorticity (ζ/f) and (bottom) geostrophic sea surface height (η_g) at the end of various simulations. Each column represents a simulation with different sea ice concentration, namely conc30 (30%, left), conc55 (55%, middle) and conc80 (80%, right). The sea ice floes are shown in gray. Colored lines within floes indicate their orientation and the sign of rotation (red: cyclonic, blue: anticyclonic). The orientation angle is only plotted if the rotation rate exceeds 0.1 day^{-1}.

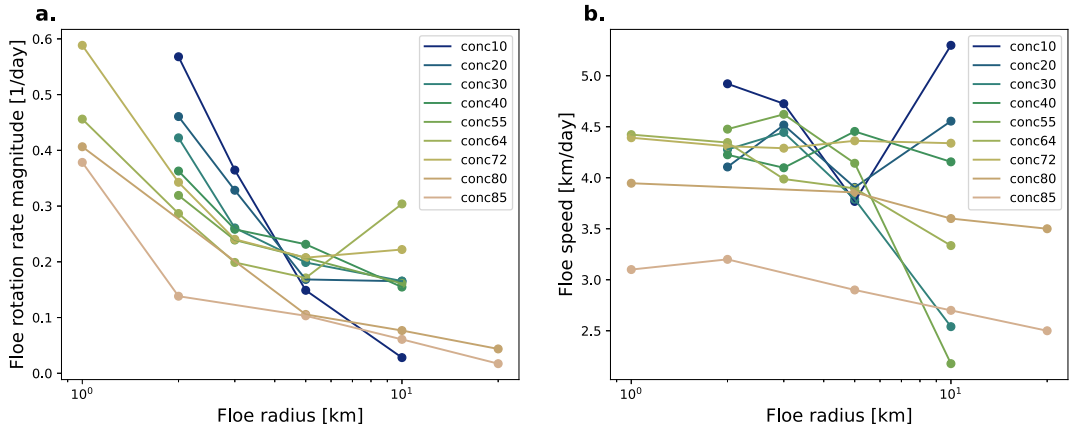

Figure 4. (a) Mean floe rotation rate and (b) mean floe speed calculated over each floe size category and averaged over the last 6 days of the simulations.

are carried by the large-scale strain field and the ice is mostly in free drift. For medium-range concentrations (conc40 to conc64), the floe speed decreases with floe radius because large floes are often trapped within mesoscale features, while smaller floes can more readily travel in between eddies. For higher sea ice concentrations (conc72), large floes can occasionally receive short-lived velocity bursts due to collisions, which explains their higher average velocity compared to the same floe sizes at intermediate sea ice concentrations. At even higher concentrations (conc80 and conc85), the floe speeds become smaller for all floe sizes due to the limited open ocean space in the domain.

We note that there is significant variability across individual floes for the floe speeds and rotation rates reported in Figure 4 (not shown). In some simulations, particularly at low sea ice concentration, the average floe speeds also depend on the starting position of floes, as it affects subsequent interactions with floes and eddies. Here, we report on floe speeds and rotation rates averaged in the last 6 days of each simulation, as the statistics do not change notably within that period. Further work using simulation ensembles would help better quantify inter-floe variability and its dependency on initial conditions.

The sign of sea ice and under-ice vorticity are also useful metrics for characterizing ice-ocean interactions and the trapping of floes by ocean eddies (Figure 5). For each simulation with resolved floes, we calculate histograms of normalized ocean vorticity under sea ice (ζ/f), recording the surface vorticity of all grid cells having at least 80% sea ice fraction. We also consider histograms of normalized sea ice vorticity, defined for each floe "k" as $2\Omega_i^k/f$. We define the parameters r_i and r_o as the ratio between the number of positive (cyclonic) and negative (anticyclonic) instances recorded in the histograms of floe vorticity and ocean vorticity under ice, respectively. At low sea ice concentration (conc10 to conc72), we find $r_i < 1$ and $r_o < 1$, representing a dominance of anticyclonic rotation (also seen in Figures 3a and 3d). Moreover, at these low concentrations, the ocean vorticity under ice has greater anticyclonic skew than the sea ice vorticity. As the concentration increases from conc10 to conc72, both r_i and r_o increase, and the shapes of the ice and ocean vorticity histograms become more Gaussian. At high concentrations (conc80 and conc85), r_i and r_o are slightly greater than 1, and the histograms become narrower, particularly for sea ice.

3.2. Sea Ice Floe Melt

We next investigate the sea ice melt rate as a function of ice concentration and floe size (Figure 6). The total volumetric melt rate divided by the horizontal domain area is representative of the surface fresh water flux and can be evaluated as follows:

$$\dot{h}_t = -\frac{1}{L^2}\frac{d}{dt}\sum_{i=1}^{N_f} h_i A_i. \tag{10}$$

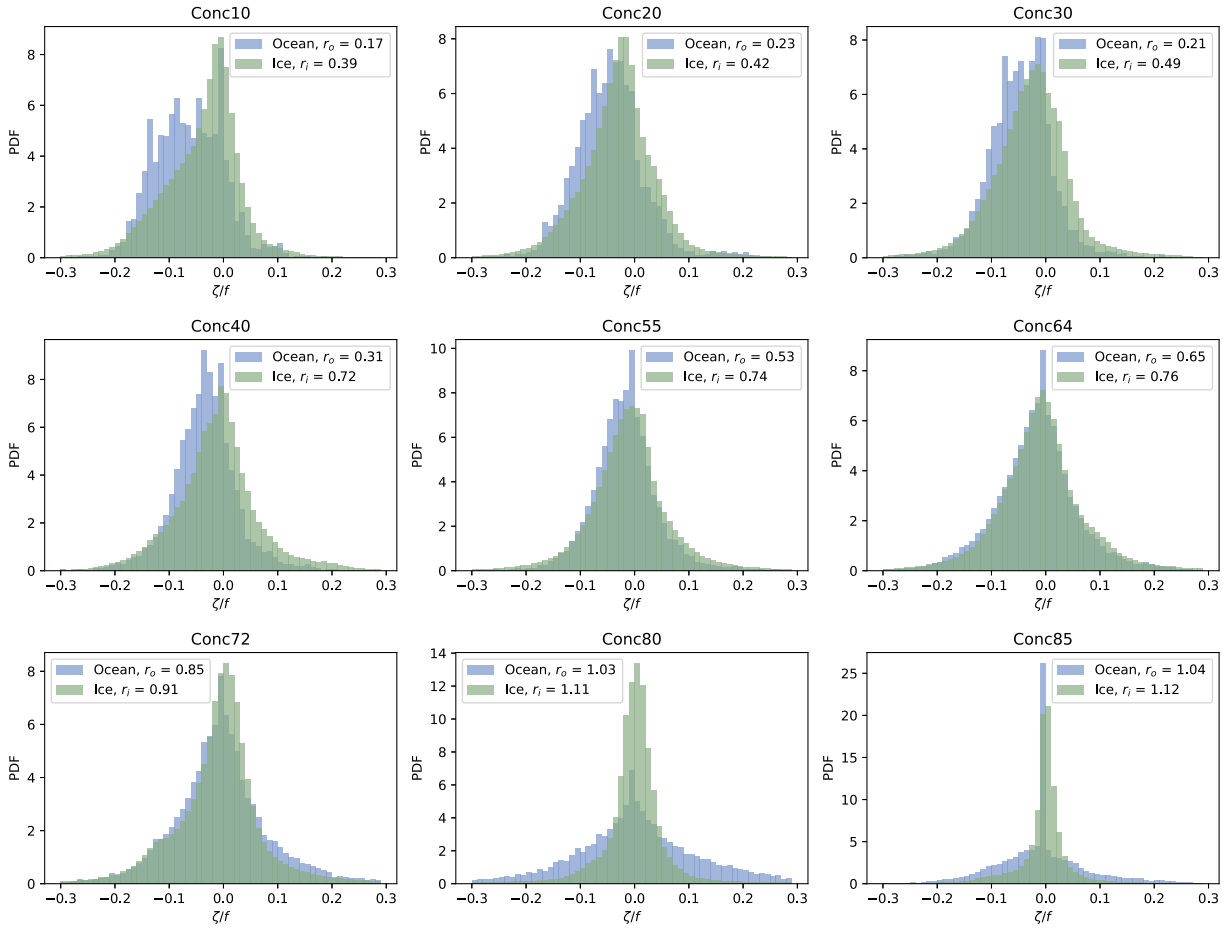

Figure 5. Normalized histograms of surface ocean relative vorticity under sea ice (ζ/f, blue) and sea ice floe vorticity ($2\Omega_i^k/f$, green) for conc10 to conc85, with 0.01 bin spacing. The parameters r_i and r_o are the ratio of positive to negative instances in the ice and ocean vorticity histograms, respectively.

$\dot{h}_t$ first increases with sea ice concentration (conc10 to conc72), as the ice mass available for melt increases. Then, between conc72 and conc100, $\dot{h}_t$ decreases with concentration, as the ice-albedo feedback reduces the net heat absorbed by the ocean, and basal melt becomes less efficient. The effect of the ice-albedo feedback can be further illustrated by evaluating the mean melt rate, defined as the volumetric melt rate normalized by the sea ice area:

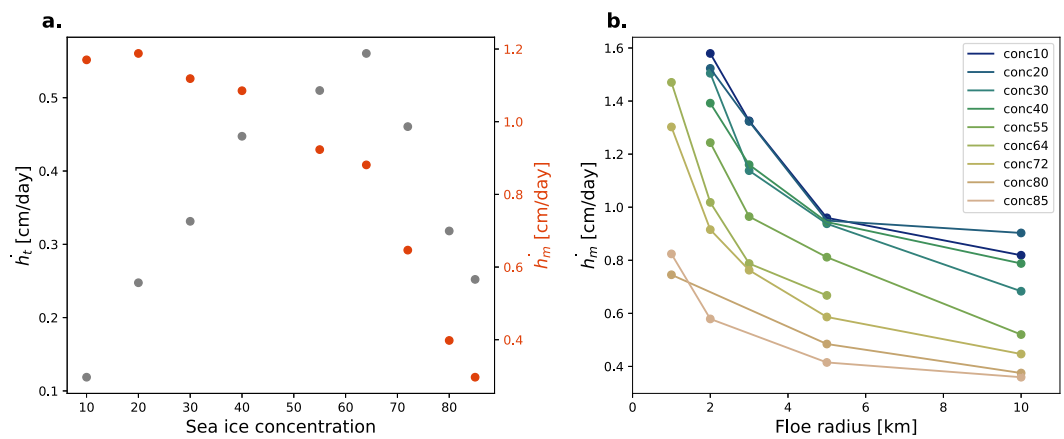

Figure 6. (a) Total melt rate ($\dot{h}_t$, gray dots, defined in Equation 10) and mean melt rate ($\dot{h}_m$, red dots, defined in Equation 11) as a function of sea ice concentration. (b) Mean melt rate averaged over each floe size category.

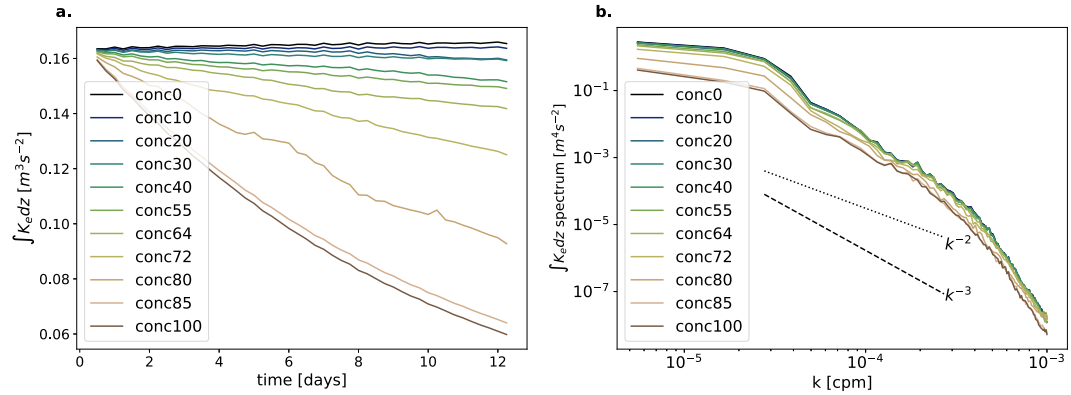

Figure 7. (a) Time series of the depth-integrated and horizontal-mean EKE after the insertion of floes for different sea ice concentrations. (b) Spectra of the depth-integrated eddy kinetic energy, K_e. The dotted and dashed lines show the k^{-2} and k^{-3} slopes, respectively.

$$\dot{h_m} = -\frac{d}{dt}\left(\frac{\sum_{i=1}^{N_f} h_i A_i}{\sum_{i=1}^{N_f} A_i}\right), \tag{11}$$

which decreases monotonically with sea ice concentration. Moreover, for all sea ice concentrations, the mean melt rate $\dot{h_m}$ evaluated separately for each floe size category tends to decrease with floe size (Figure 6b). This size-dependent melt rate is consistent with previous studies, which show that the lateral supply of heat toward ice floes is mediated by mixed layer eddies and is most effective for smaller floes (Gupta & Thompson, 2022; Horvat et al., 2016).

3.3. EKE Budget

Here, we examine changes to the ocean's energy content due to the presence of sea ice floes. We define the EKE as:

$$K_e = \frac{1}{2}\left(\overline{u'u'} + \overline{v'v'}\right), \tag{12}$$

where we have dropped the subscript "o" in describing ocean velocities. Anomalies here and elsewhere are taken with respect to the horizontal-mean at each time step. Due to the structure of the wind forcing used to generate ocean eddies (Equation 8), there is no mean current in our simulations, and the velocity anomalies are equal to the total velocity.

The presence of sea ice reduces the depth-integrated energy content of the ocean (Figure 7a). For conc100, the EKE declines by a factor of 63% in the span of 12 days, while it only declines by 12% for conc64, for example. The difference in EKE trend between conc85 and conc100 is small, reflecting the fact that floes already become strongly restricted in their motions at 85% concentration, leading to substantial ice-ocean friction. This concentration threshold may be affected by the idealized geometry of the floes and the lack of breakage and ridging processes.

We also assess the slope of the depth-integrated EKE spectrum over characteristic mesoscale ($10^{-5} < k < 10^{-4}$ cpm) and sub-mesoscale ($10^{-4} < k < 10^{-3}$ cpm) ranges, which distinguishes features that are approximately larger and smaller than R_d, respectively (Figure 7b). Over the mesoscale range, the slopes of the spectra do not vary substantially across simulations, with a value ranging from $k^{-3.5}$ between conc0 to conc64, and k^{-3} for conc80 to conc100. In the sub-mesoscale range, the slope of the EKE spectrum remains at $k^{-5.9}$ for all simulations.

The relative contributions of EKE dissipation and production can be isolated by performing a horizontally-averaged and depth-integrated EKE budget based on the following balance:

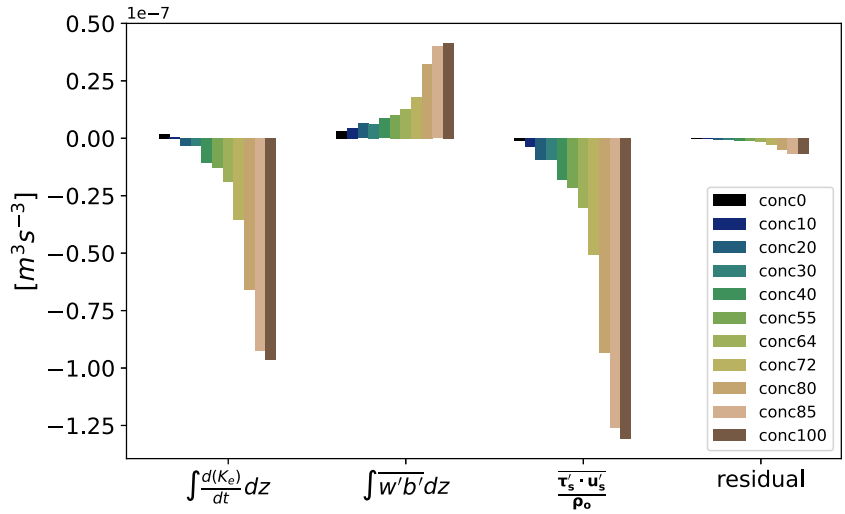

Figure 8. Depth-integrated and horizontally-averaged EKE budget based on Equation 13 for each of the simulations. From left-to-right, the terms represent EKE tendency, baroclinic production, ice-ocean frictional dissipation, and the budget residual.

$$\int \frac{dK_e}{dt}\, dz = \int \overline{w'b'}\, dz + \frac{\overline{\boldsymbol{\tau}_s' \cdot \boldsymbol{u}_s'}}{\rho_o} + \int \epsilon\, dz, \tag{13}$$

where $b = -g(\rho - \rho_o)/\rho_o$ is the buoyancy, $\boldsymbol{\tau}_s$ is the net stress on the ocean surface, $\boldsymbol{u}_s'$ is the surface ocean velocity, and ϵ is numerical dissipation. The term $\left(\overline{\boldsymbol{\tau}_s' \cdot \boldsymbol{u}_s'}\right)/\rho_o$ represents energy dissipation due to ice-ocean friction, while $\overline{w'b'}$ represents baroclinic conversion of potential energy into EKE. Terms corresponding to EKE transport do not appear in the budget due to the doubly periodic boundary conditions and the depth integration, while the term representing shear production of EKE is absent due to the lack of a mean ocean current. The EKE budget is evaluated online at every time step and shown in Figure 8. The numerical dissipation is inferred as a residual from the other terms, and provides a small negative contribution to the EKE budget. In what follows, "dissipation" will refer exclusively to EKE loss due to ice-ocean friction.

The trend in K_e is negative for all experiments containing floes, and increases in magnitude with sea ice concentration, reflecting the net effect of sea ice on damping EKE. This decline in EKE is driven by the ice-ocean stress, which is significant even when floes are largely in free drift (<conc80), consistent with the results of Brenner et al. (2023). Between conc80 and conc100, damping increases rapidly as floes become more interlocked and are less frequently in free drift. However, the dissipation of EKE by ice-ocean friction is partially compensated by baroclinic production $\left(\overline{w'b'}\right)$ in all simulations containing sea ice. This compensation ranges from 69% to 30% of the dissipation magnitude for conc30 to conc100, respectively, and thus impacts the depth-integrated budget significantly. In the following sections, we discuss the processes governing baroclinic energy production under sea ice and how they differ between the upper-ocean and the shallow surface melt layer.

3.4. Baroclinic Energy Production in the Upper Ocean

Examining depth profiles of the EKE tendency and baroclinic energy production helps to disentangle the relative roles of sea ice in kinetic energy dissipation and production. EKE loss due to sea ice is largely concentrated within the top ∼50 m of the domain (Figure 9), which corresponds approximately to the "upper-layer" bounded by the peak in stratification at 41 m, as defined in Section 2.3. Ice-ocean friction is only directly felt by the topmost grid level of the model, but energy loss is communicated deeper in the water column via vertical mixing induced by eddies. This mixing is suppressed in the highly stratified waters between 25 and 50 m, and the energy loss is not communicated below 50 m.

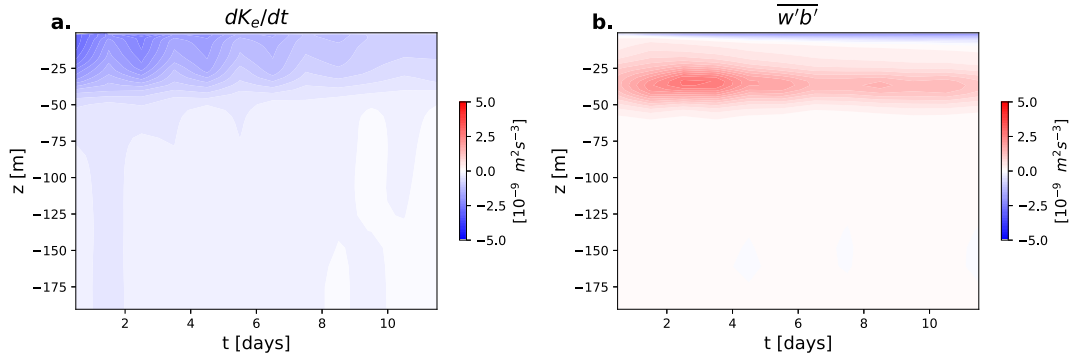

Figure 9. Hovmöller plots of the horizontal-mean (a) EKE tendency and (b) baroclinic production $\overline{w'b'}$ for conc100.

Baroclinic energy production $\left(\overline{w'b'}\right)$ is net positive between approximately 5 and 50 m, and negligible below that depth (Figure 9). Positive baroclinic energy production below 5 m is observed in all simulations containing sea ice, but is strongest for larger ice concentrations (not shown). In the near-surface (top 5 m), $\overline{w'b'}$ is additionally affected by sea ice melt, and may be positive or negative depending on the sea ice concentration. In this section, we focus on processes controlling baroclinic EKE production within the upper-ocean (top 50 m), while in Section 3.5, we discuss dynamics occurring within the shallow melt layer (top 5 m).

It is instructive to investigate depth profiles of the root-mean-square (RMS) buoyancy $\left(b_{rms} = \sqrt{b'^2}\right)$ and vertical velocity $\left(w_{rms} = \sqrt{w'^2}\right)$ to better understand the structure of $\overline{w'b'}$ shown in Figure 9. b_{rms} has a peak around 40 m depth (Figure 10a), which coincides with a peak in N^2 (Figure 1d) and locations of positive $\overline{w'b'}$ (Figure 9b). As the sea ice concentration increases, both w_{rms} and b_{rms} decrease in magnitude, due to the decline in horizontal EKE, which likely reduces frontogenesis and ageostrophic motions. We thus find that w_{rms} and b_{rms} decrease in magnitude (Figure 10) while $\overline{w'b'}$ increases in magnitude (Figure 8) for increasing sea ice concentration. This implies that the correlation between b and w must increase with sea ice concentration.

We probe the correlation between b and w by examining their vertical profiles averaged within cyclonic $(\zeta > \zeta_{rms})$, anticyclonic $(\zeta < -\zeta_{rms})$ and low-vorticity $(|\zeta| < \zeta_{rms})$ regions for conc0 and conc100 (Figure 11). The threshold $\zeta_{rms} = \sqrt{\zeta'^2}$ separating cyclonic versus anticyclonic features is computed from the surface anomalies of the relative vorticity for each time step. For conc0, ζ_{rms}/f is 0.042 and constant in time, while for conc100 it reduces from 0.042 to 0.024 during the course of the simulation, as its energy content declines. Using

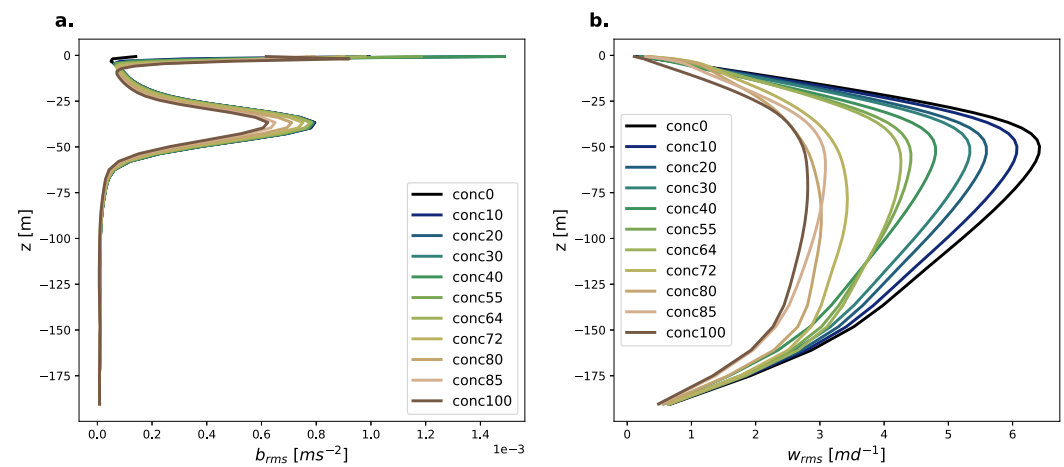

Figure 10. Horizontally-averaged profiles of (a) b_{rms} and (b) w_{rms}.

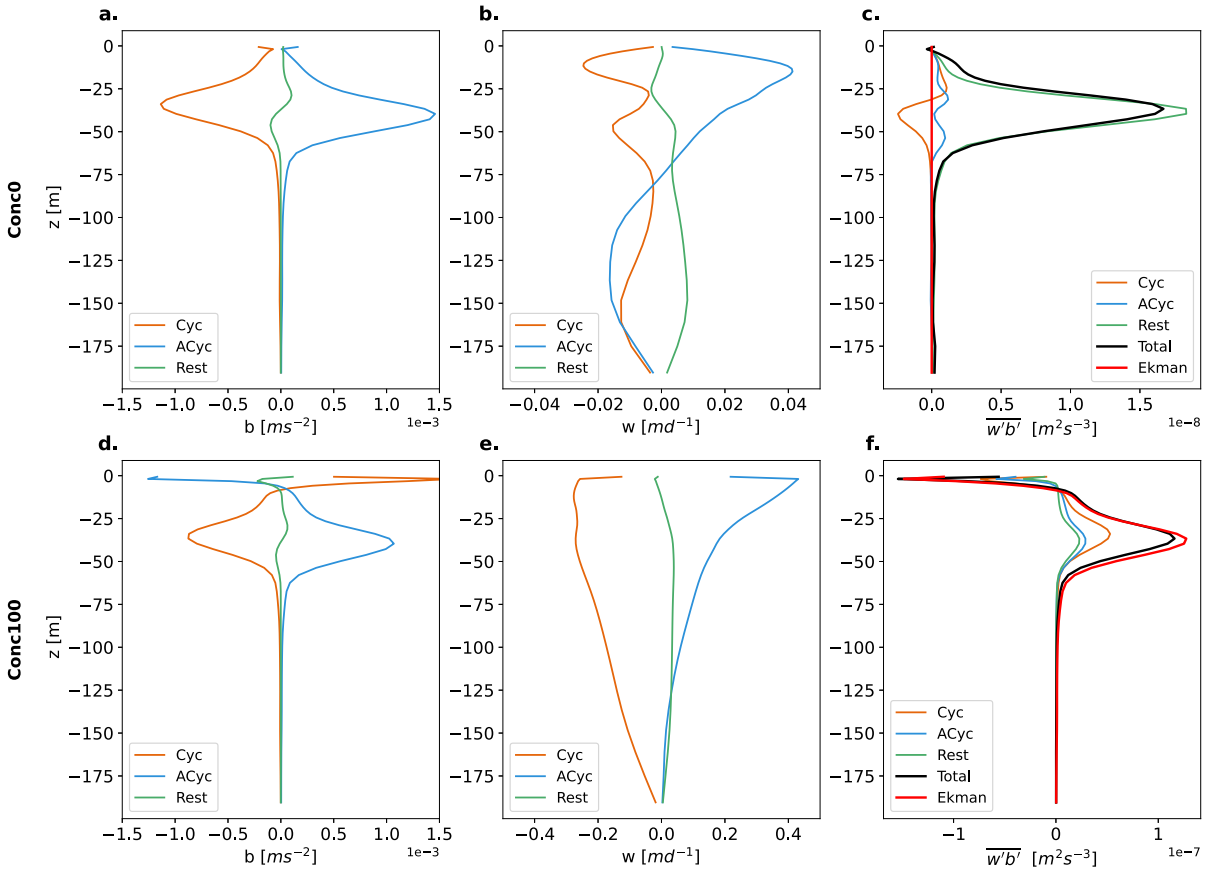

Figure 11. Profiles of (left) b (middle) w and (right) $\overline{w'b'}$ averaged over cyclonic ($\zeta > \zeta_{rms}$, orange), anticyclonic ($\zeta < -\zeta_{rms}$, blue), and low vorticity ($|\zeta| < \zeta_{rms}$, green) regions. The top row (a–c) is for conc0 and the bottom row (d–f) is for conc100. Note the different scales for panels (b, e) and panels (c, f), respectively, reflecting the larger values of w and $\overline{w'b'}$ for conc100 relative to conc0. Panels (c, f) additionally contain profiles of $\overline{w_{ek}b'}$ in red.

this threshold, the areal fractions of cyclonic, anticyclonic and low-vorticity regions are approximately 18%, 15% and 67%, respectively, in both simulations.

In conc0 (top row of Figure 11), the baroclinic energy production $\overline{w'b'}$ is relatively small in magnitude and its contribution is dominated by low-vorticity regions. Between 25 and 60 m, b and w are on average negative within cyclones and positive within anticyclones, reflecting a warm and salty versus a cold and fresh core, respectively. However, the correlation between b and w is weak inside these high-vorticity regions, leading to low values of $\overline{w'b'}$. By contrast, when averaging within low-vorticity regions, b and w are individually small, but they are more tightly correlated with each other, and thus these regions contribute most strongly to $\overline{w'b'}$.

In conc100 (bottom row of Figure 11), the baroclinic energy production $\overline{w'b'}$ is approximately 10 times greater than in conc0, with significant contributions from cyclones, anticyclones and low-vorticity regions. The buoyancy profiles have comparable magnitude between conc0 and conc100, but the vertical velocity is approximately 10 times larger in conc100 when averaged over cyclones and anticyclones, respectively. This large enhancement in the vertical velocities is attributed to Ekman pumping and suction driven by ice-ocean friction, and the term $\overline{w'b'}$ is well approximated by $\overline{w_{ek}b'}$, where

$$w_{ek} = \frac{1}{\rho_o f}\hat{z} \cdot \nabla \times \boldsymbol{\tau_s} \tag{14}$$

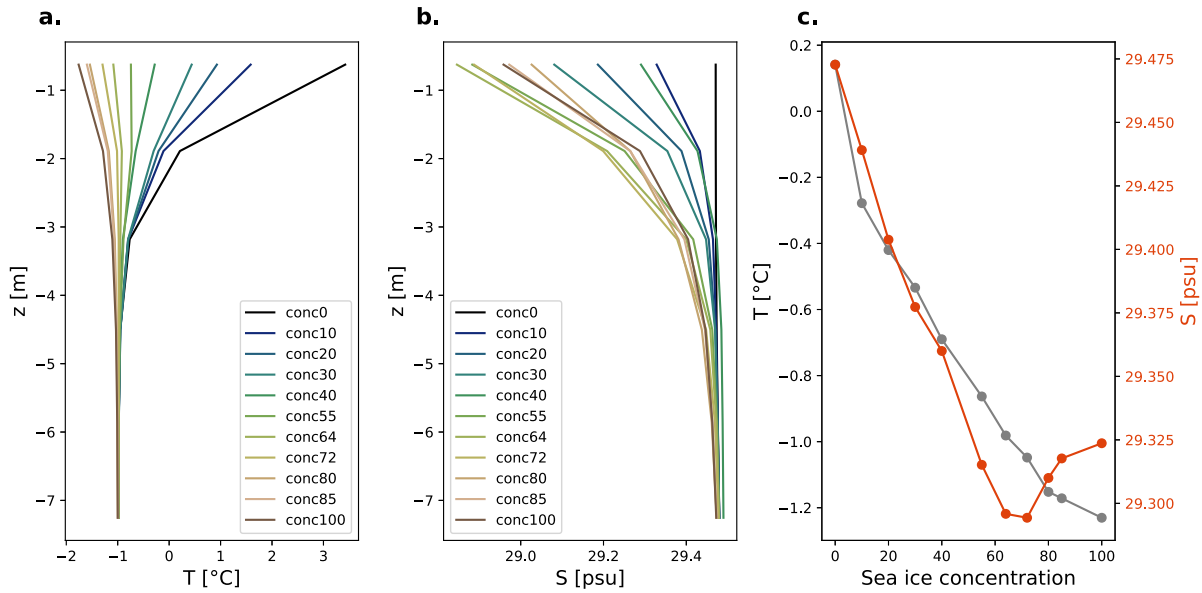

Figure 12. (a, b) Horizontally-averaged profiles within the melt layer for (a) temperature and (b) salinity. (c) Temperature (gray) and salinity (red) averaged in the top 5 m of the ocean.

is the vertical Ekman velocity and $\hat{z}$ is a unit vector pointing upward. The enhanced vertical velocities due to Ekman pumping and suction are thus localized and coincide with regions of significant buoyancy anomalies near the core of eddies, leading to rectified baroclinic energy production. This $\overline{w'b'}$ is strongest between the mixed layer and the peak in the stratification profile (∼20–50 m). Below this layer, the horizontal buoyancy anomalies are negligible, and above it, the stratification (and thus the potential energy content) is too weak to generate significant EKE, except in the shallow melt layer discussed in the next section.

3.5. Energetics of the Shallow Melt Layer

In the near-surface, baroclinic energy production is strongly affected by melt, in addition to the Ekman dynamics discussed in Section 3.4. Sea ice melt produces a cold and fresh layer spanning approximately 5 m depth, with the rest of the temperature and salinity profiles being largely unaffected (Figure 12). Within this shallow melt layer, the temperature declines monotonically with increasing sea ice concentration, displaying surface values ranging from +3°C to −2°C for conc0 and conc100, respectively. The salinity averaged over the top 5 m first declines with sea ice concentration (between conc0 and conc55), and then increases slightly with concentration (between conc72 and conc100), consistent with the fresh water flux $\left(\dot{h}_t\right)$ reported in Figure 6a.

In the topmost model layer, $\overline{w'b'}$ is zero for conc0 and increases between conc0 and conc40, due to the generation of mixed layer eddies from inhomogeneous sea ice melt (Figure 13a). At these low concentrations, the space between floes allows the formation of distinct melt clusters, as illustrated by the increase in the horizontal buoyancy gradient magnitude averaged over the surface ($\overline{|\nabla_h b|}$). Between conc40 and conc80, $\overline{w'b'}$ remains positive but declines in magnitude, together with $\overline{|\nabla_h b|}$. Between conc80 and conc100, $\overline{|\nabla_h b|}$ continues to decline and $\overline{w'b'}$ becomes negative, reflecting mixing suppression due to sea ice melt, which reduces local buoyancy anomalies and vertical velocities (top 5 m in Figure 9b). At high concentrations, the increase in the stratification thus reinforces the effect of ice-ocean friction in damping kinetic energy. The surface EKE tendency (dK_e/dt) is always negative and declines monotonically with sea ice concentration. We do not plot the frictional dissipation term in Figure 13a because it is significantly greater in magnitude than $\overline{w'b'}$ and dK_e/dt over the surface model layer, but it is largely balanced by the vertical exchange of EKE with layers below.

The changes in surface EKE due to sea ice are not uniformly distributed across scales (Figure 13b). Over the mesoscale range ($10^{-5} < k < 10^{-4}$ cpm), the EKE content declines with sea ice concentration, with a substantial jump from conc80 to conc85, but the slopes of the spectra remain approximately k^{-2} for all simulations. In the

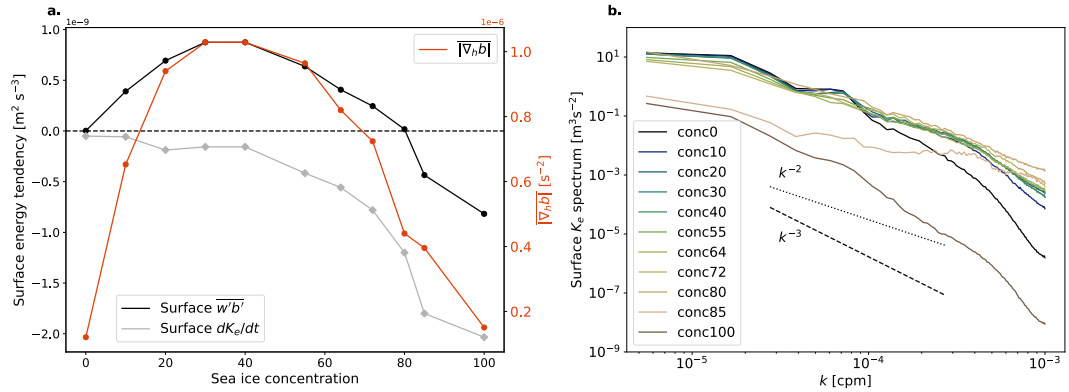

Figure 13. (a) Surface-averaged $\overline{w'b'}$ (black), dK_e/dt (gray), and $\overline{|\nabla_h b|}$ (red) as a function of sea ice concentration. (b) Surface EKE spectra for different sea ice concentrations (colors). The dotted and dashed lines show the k^{-2} and k^{-3} slopes, respectively.

sub-mesoscale range ($10^{-4} < k < 10^{-3}$ cpm), the slope of the EKE spectrum increases sharply from $k^{-5.2}$ to $k^{-1.6}$ between conc0 and conc85. Moreover, from conc10 to conc80, the integrated energy content in the sub-mesoscale range exceeds that from conc0. As the concentration increases beyond conc80, the EKE content in the sub-mesoscale range declines due to a combination of frictional dissipation, reduced $\overline{|\nabla_h b|}$, and mixing suppression from increased stratification. For conc100, the surface EKE spectrum recovers a shape similar to that in conc0, but with lower energy at all scales.

4. Discussion

Our simulations reveal two distinct mechanisms giving rise to baroclinic production of EKE in the presence of sea ice (Figure 14): (a) Ekman-induced vertical velocities due to ice-ocean friction generate upwelling within cold and fresh anticyclones and downwelling within warm and salty cyclones. The resulting baroclinic energy production is concentrated between the base of the mixed layer and a characteristic peak in the stratification profile (20–50 m, Figure 9), and can inject energy at the mesoscale. This mechanism is analogous to Eddy Ice Pumping

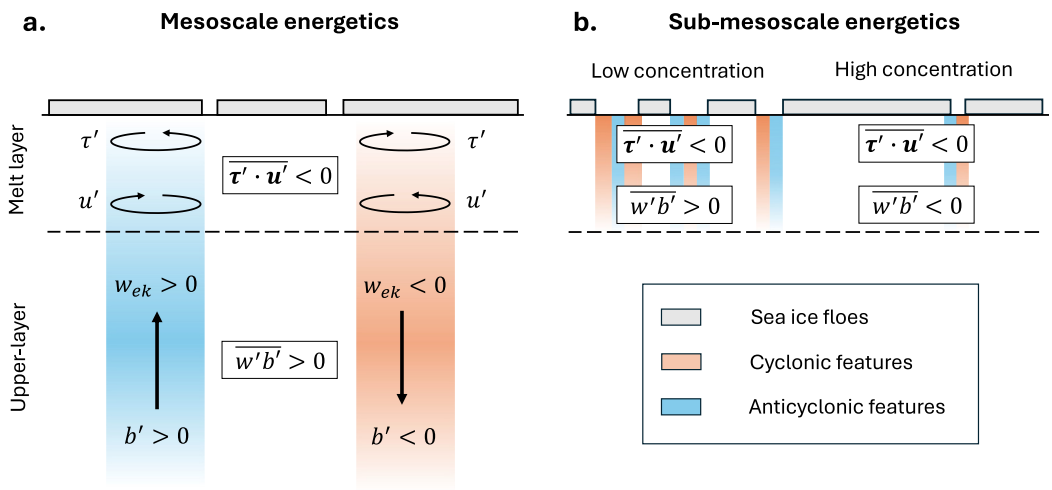

Figure 14. Schematic of the upper-ocean energetics under sea ice discussed in this work. (a) At the mesoscale, ocean eddies rubbing against sea ice cause EKE dissipation $(\overline{\tau' \cdot u'} < 0)$, which is partially compensated by baroclinic EKE production $(\overline{w'b'} > 0)$ due to Ekman pumping in cyclones and Ekman suction in anticyclones. (b) At the sub-mesoscale, for low sea ice concentrations, lateral buoyancy gradients due to sea ice melt generate EKE $(\overline{w'b'} > 0)$ in the surface melt layer. At higher sea ice concentrations, the increased stratification due to melt reduces EKE in favor of potential energy $(\overline{w'b'} < 0)$.

(Gupta et al., 2020; Huot et al., 2022), where Ekman-induced vertical heat fluxes under compacted sea ice can cause rectified basal sea ice melt during fall and winter. In our simulations, under summer-like conditions, the Ekman-driven vertical heat fluxes are small compared to the net heat flux at the top of sea ice, but the corresponding buoyancy fluxes are significant for the column-integrated EKE budget (Figure 8). (b) Buoyancy gradients arising from inhomogeneous sea ice melt can generate mixed layer eddies, which enhance sub-mesoscale baroclinic energy production in the shallow melt layer (top 5 m), accelerate sea ice melt (Gupta & Thompson, 2022; Horvat et al., 2016), but do not contribute substantially to the depth-integrated EKE budget. Mixed layer eddy generation peaks at intermediate sea ice concentration (conc40), consistent with the strongest lateral buoyancy gradients at the surface. For higher sea ice concentrations (conc80 to conc100), the surface $\overline{w'b'}$ is negative due to mixing suppression induced by increased stratification, and thus reinforces the effect of frictional dissipation in the shallow surface layer.

Despite distinct energy production mechanisms under sea ice, the primary effect of the ice cover in our simulations remains the damping of EKE due to ice-ocean friction. This reduction in EKE under sea ice is consistent with observations (Cassianides et al., 2023; Manucharyan et al., 2022) and models (Li et al., 2024; Muller et al., 2024) of the Arctic Ocean, which also show the strongest kinetic energy damping near the surface. Meneghello et al. (2021) further argue that friction from a thick ice cover can reduce eddy growth rates in the near-surface by dissipating vorticity and reducing the potential for baroclinic instability. This effect is distinct from the enhanced Ekman-induced production under ice discussed here, which occurs at the scale of individual eddies. In our simulations, the absence of a mean vertical velocity shear and the associated isopycnal gradients precludes the spontaneous generation of a mesoscale field, which is instead initialized via winds that have spatial variability at the ocean mesoscale. Future work should investigate how the interactions explored here may differ for eddies produced under more realistic conditions, since the size, vertical extent, polarity and thermodynamic properties of eddies can vary substantially within the Arctic Ocean (Cassianides et al., 2023; Planat et al., 2025; Zhao et al., 2014) and in the Southern Ocean (Hausmann et al., 2017; Kosty et al., 2025).

Beyond the total EKE content, the presence of sea ice may affect EKE distribution across scales. At the surface, we find that the slope of the EKE spectrum in the mesoscale range is approximately k^{-2} and does not vary substantially with sea ice concentration, while the slope in the sub-mesoscale range increases from $k^{-5.2}$ to $k^{-1.6}$ between conc0 and conc85. Mensa and Timmermans (2017) find an EKE slope varying between k^{-2} during the summer and k^{-3} in winter, and attribute the stronger sub-mesoscale activity in summer to wind-forced internal wave activity in the absence of ice. On the other hand, Manucharyan and Thompson (2022) find a k^{-4} slope in the summer and a k^{-1} slope in the winter, and attribute the increased presence of sub-mesoscales in the winter to mesoscale-driven frontogenesis and brine-induced convection. In the present work, we do not consider winter-like conditions and the associated freezing process. Moreover, our explicit representation of floes differs from these past studies, and likely allows for sharper horizontal gradients due to melt compared to continuum sea ice models. These factors, along with different model resolutions and experimental setups, could help explain the distinct seasonal behaviors in the EKE slope, but further work is required to reconcile them. More detailed comparisons with observationally-derived energetic properties would also be beneficial, but this remains challenging, given the sparseness of the data and the large range of energetic regimes observed under Arctic sea ice (Cassianides et al., 2023).

The spatial distribution of floes in our simulations is primarily governed by the surface mesoscale oceanic circulation and leads to an aggregation of floes outside the core of large eddies. This behavior is consistent with the reported dispersion of particles at the surface of the ocean by the large-scale strain field (Maalouly et al., 2023) and the expulsion of floes out of high-vorticity regions due to radial imbalance (Gupta et al., 2024; Zhang et al., 2015). At low sea ice concentration (conc10 to conc72), the dominant sense of floe rotation is anticyclonic, consistent with observations in the Arctic MIZ (Manucharyan et al., 2022). The preference for anticyclonic rotation may be caused by the formation of a fresh lens under sea ice, which generates anticyclonic rotation due to thermal wind balance (Gupta & Thompson, 2022). Nevertheless, other processes, such as winds, floe-floe collisions (Herman, 2012), and convergence due to mesoscale eddies and horizontal Ekman currents (Manucharyan & Thompson, 2017) also impact floe aggregation. The spatial organization of the floes likely affects the scales of EKE injection and dissipation, sea ice melt rates, and the Ekman dynamics emphasized in this work. This behavior should therefore be accounted for in floe-aware parameterizations designed for continuum sea ice models.

The modeling framework employed in this analysis excludes several processes that are relevant for (sub-) mesoscale ice-ocean interactions in the MIZ. Winds are not considered, but can likely enhance the vertical mixing of fresh water at the surface, and suppress sub-mesoscale activity by homogenizing buoyancy anomalies in the shallow melt layer (Swart et al., 2020). Localized wind events may also disrupt the spatial distribution of floes by eddies and accelerate melt by transporting floes outside of their cold water lens (Gupta & Thompson, 2022). The sea ice model is also highly idealized; notably, it does not include breakage, which can play a dominant role in the evolution of the FSD between spring and summer (Bateson et al., 2020; Moncada et al., 2023). The round floe shapes also limit the exploration of tightly packed sea ice conditions with resolved floes and may underestimate interlocking behavior (Dansereau et al., 2017; West et al., 2022; Wilchinsky & Feltham, 2006). Irregular floe shapes may notably affect the concentration threshold at which sea ice is no longer in free drift, for both translational and rotational motions, and thus alter the frictional dissipation of EKE. Furthermore, including features such as snow and melt ponds, would increase the realism of our model and help validate the simulated behavior against observations.

5. Conclusions

This study investigates the energetics of the upper-ocean in the presence of sea ice using simulations of decaying ocean turbulence. We find that the dissipation of oceanic eddy kinetic energy (EKE) due to ice-ocean friction is partially compensated by baroclinic energy production $\left(\overline{w'b'}\right)$ driven by Ekman pumping and suction within mesoscale eddies (Figure 14). These vertical motions are co-located with buoyancy anomalies at the core of cyclones and anticyclones, leading to a release of EKE. Integrated over the modeled ocean depth, baroclinic production accounts for 69%–30% of the dissipation magnitude for sea ice concentrations varying between 30% and 100%, respectively. The dissipation of EKE is surface-intensified, while baroclinic production occurs below the mixed layer, where it may impact exchanges with the halocline. This result highlights the importance of mesoscale ice-ocean interactions in capturing upper-ocean properties and mixing under sea ice, which are typically not well represented by existing climate models and parameterizations.

Near the surface, our simulations generate a shallow melt layer (∼5 m) that is consistent with observations under sea ice (Nomura et al., 2023; Smith et al., 2023, 2025). For sea ice concentrations typical of marginal ice zones (<80%), the heterogeneous melting of sea ice floes generates horizontal buoyancy gradients that energize turbulence within the shallow surface layer and substantially reduce the slope of the EKE spectrum in the sub-mesoscale range. Consistent with past work using more idealized model configurations (Gupta & Thompson, 2022; Horvat et al., 2016), sea ice melt rates decrease with increasing floe size, due to mixed-layer ocean turbulence mediating their access to basal heat. Moreover, surface eddies aggregate floes into distinct clusters, whose spatial organization can modulate the effective sea ice rheology, floe melt rates, sub-mesoscale energy production in the melt layer, and frictional interactions with the mesoscale field that extends at depth. These coupled processes are likely not appropriately captured by continuum sea ice models, even when operating at high resolution (Brenner et al., 2023; Shrestha & Manucharyan, 2022), motivating the need to develop more advanced floe-aware parameterizations of sea ice dynamics.

Conflict of Interest

The authors declare no conflicts of interest relevant to this study.

Data Availability Statement

The sea ice floe code is provided in Gupta (2022), "Oceananigans.jl" is available in Ramadhan et al. (2020), and the simulation data is available in Gupta (2025).

Acknowledgments
M.G. and A.F.T. acknowledge the support of the Office of Naval Research Multidisciplinary University Research Initiative (MURI) on Mathematics and Data Science for Physical Modeling and Prediction of Sea Ice, N00014-23-1-2014. We also thank two anonymous reviewers, whose thoughtful comments helped improve the manuscript.

References

Arrigo, K. R. (2014). Sea ice ecosystems. *Annual Review of Marine Science*, *6*(1), 439–467. https://doi.org/10.1146/annurev-marine-010213-135103

Åström, J., Robertsen, F., Haapala, J., Polojärvi, A., Uiboupin, R., & Maljutenko, I. (2024). A large-scale high-resolution numerical model for sea-ice fragmentation dynamics. *The Cryosphere*, *18*(5), 2429–2442. https://doi.org/10.5194/tc-18-2429-2024

Bateson, A. W., Feltham, D. L., Schröder, D., Hosekova, L., Ridley, J. K., & Aksenov, Y. (2020). Impact of sea ice floe size distribution on seasonal fragmentation and melt of arctic sea ice. *The Cryosphere*, *14*(2), 403–428. https://doi.org/10.5194/tc-14-403-2020

Boutin, G., Williams, T., Rampal, P., Olason, E., & Lique, C. (2021). Wave–sea-ice interactions in a brittle rheological framework. *The Cryosphere*, *15*(1), 431–457. https://doi.org/10.5194/tc-15-431-2021

Brannigan, L., Marshall, D. P., Naveira-Garabato, A., & George Nurser, A. (2015). The seasonal cycle of submesoscale flows. *Ocean Modelling*, *92*, 69–84. https://doi.org/10.1016/j.ocemod.2015.05.002

Brenner, S., & Horvat, C. (2024). Scaling simulations of local wind-waves amid sea ice floes. *Journal of Geophysical Research: Oceans*, *129*(12), e2024JC021629. https://doi.org/10.1029/2024JC021629

Brenner, S., Horvat, C., Hall, P., Lo Piccolo, A., Fox-Kemper, B., Labbé, S., & Dansereau, V. (2023). Scale-dependent air-sea exchange in the polar oceans: Floe-Floe and floe-flow coupling in the generation of ice-ocean boundary layer turbulence. *Geophysical Research Letters*, *50*(23), e2023GL105703. https://doi.org/10.1029/2023GL105703

Callies, J., Flierl, G., Ferrari, R., & Fox-Kemper, B. (2016). The role of mixed-layer instabilities in submesoscale turbulence. *Journal of Fluid Mechanics*, *788*, 5–41. https://doi.org/10.1017/jfm.2015.700

Cassianides, A., Lique, C., Tréguier, A.-M., Meneghello, G., & De Marez, C. (2023). Observed spatio-temporal variability of the eddy-sea ice interactions in the arctic basin. *Journal of Geophysical Research: Oceans*, *128*(6), e2022JC019469. https://doi.org/10.1029/2022JC019469

Cocetta, F., Zampieri, L., Selivanova, J., & Iovino, D. (2024). Assessing the representation of arctic sea ice and the marginal ice zone in ocean–sea ice reanalyses. *The Cryosphere*, *18*(10), 4687–4702. https://doi.org/10.5194/tc-18-4687-2024

Cohanim, K., Zhao, K. X., & Stewart, A. L. (2021). Dynamics of eddies generated by sea ice leads. *Journal of Physical Oceanography*, *51*(10), 3071–3092. https://doi.org/10.1175/JPO-D-20-0169.1

Comiso, J. C. (2012). Large decadal decline of the arctic multiyear ice cover. *Journal of Climate*, *25*(4), 1176–1193. https://doi.org/10.1175/JCLI-D-11-00113.1

Dansereau, V., Weiss, J., Saramito, P., Lattes, P., & Coche, E. (2017). Ice bridges and ridges in the Maxwell-EB sea ice rheology. *The Cryosphere*, *11*(5), 2033–2058. https://doi.org/10.5194/tc-11-2033-2017

Denton, A. A., & Timmermans, M.-L. (2022). Characterizing the sea-ice floe size distribution in the Canada basin from high-resolution optical satellite imagery. *The Cryosphere*, *16*(5), 1563–1578. https://doi.org/10.5194/tc-16-1563-2022

Dumont, D. (2022). Marginal ice zone dynamics: History, definitions and research perspectives. *Philosophical Transactions of the Royal Society A: Mathematical, Physical and Engineering Sciences*, *380*(2235), 20210253. https://doi.org/10.1098/rsta.2021.0253

Ferrari, R., Jansen, M. F., Adkins, J. F., Burke, A., Stewart, A. L., & Thompson, A. F. (2014). Antarctic sea ice control on ocean circulation in present and glacial climates. *Proceedings of the National Academy of Sciences*, *111*(24), 8753–8758. https://doi.org/10.1073/pnas.1323922111

Gupta, M. (2022). Sea ice circular floe code [Software]. *Zenodo*. https://doi.org/10.5281/zenodo.6578706

Gupta, M. (2025). Energetics of the upper-ocean under sea ice: Frictional dissipation versus baroclinic production [Dataset]. *Zenodo*. https://doi.org/10.5281/zenodo.17901530

Gupta, M., Gürcan, E., & Thompson, A. F. (2024). Eddy-induced dispersion of sea ice floes at the marginal ice zone. *Geophysical Research Letters*, *51*(2), e2023GL105656. https://doi.org/10.1029/2023GL105656

Gupta, M., Marshall, J., Song, H., Campin, J.-M., & Meneghello, G. (2020). Sea-ice melt driven by ice-ocean stresses on the mesoscale. *Journal of Geophysical Research: Oceans*, *125*(11), e2020JC016404. https://doi.org/10.1029/2020JC016404

Gupta, M., Regan, H., Koo, Y., Chua, S. M. T., Li, X., & Heil, P. (2025). Inferring the seasonality of sea ice floes in the Weddell Sea using ICESAT-2. *The Cryosphere*, *19*(3), 1241–1257. https://doi.org/10.5194/tc-19-1241-2025

Gupta, M., & Thompson, A. F. (2022). Regimes of sea-ice floe melt: Ice-ocean coupling at the submesoscales. *Journal of Geophysical Research: Oceans*, *127*(9), e2022JC018894. https://doi.org/10.1029/2022JC018894

Hausmann, U., McGillicuddy, D. J., Jr., & Marshall, J. (2017). Observed mesoscale eddy signatures in Southern Ocean surface mixed-layer depth. *Journal of Geophysical Research: Oceans*, *122*(1), 617–635. https://doi.org/10.1002/2016JC012225

Herman, A. (2012). Influence of ice concentration and floe-size distribution on cluster formation in sea-ice floes. *Open Physics*, *10*(3), 715–722. https://doi.org/10.2478/s11534-012-0071-6

Herman, A. (2013). Numerical modeling of force and contact networks in fragmented sea ice. *Annals of Glaciology*, *54*(62), 114–120. https://doi.org/10.3189/2013AoG62A055

Herman, A. (2016). Discrete-element bonded-particle sea ice model design, version 1.3a—Model description and implementation. *Geoscientific Model Development*, *9*(3), 1219–1241. https://doi.org/10.5194/gmd-9-1219-2016

Herman, A. (2018). Wave-induced surge motion and collisions of sea ice floes: Finite-floe-size effects. *Journal of Geophysical Research: Oceans*, *123*(10), 7472–7494. https://doi.org/10.1029/2018JC014500

Horvat, C., Roach, L. A., Tilling, R., Bitz, C. M., Fox-Kemper, B., Guider, C., et al. (2019). Estimating the sea ice floe size distribution using satellite altimetry: Theory, climatology, and model comparison. *The Cryosphere*, *13*(11), 2869–2885. https://doi.org/10.5194/tc-13-2869-2019

Horvat, C., Tziperman, E., & Campin, J.-M. (2016). Interaction of sea ice floe size, ocean eddies, and sea ice melting. *Geophysical Research Letters*, *43*(15), 8083–8090. https://doi.org/10.1002/2016GL069742

Huot, P.-V., Kittel, C., Fichefet, T., Jourdain, N. C., & Fettweis, X. (2022). Effects of ocean mesoscale eddies on atmosphere–sea ice–ocean interactions off Adélie Land, East Antarctica. *Climate Dynamics*, *59*(1), 41–60. https://doi.org/10.1007/s00382-021-06115-x

Kashiwase, H., Ohshima, K. I., Nihashi, S., & Eicken, H. (2017). Evidence for ice-ocean albedo feedback in the Arctic Ocean shifting to a seasonal ice zone. *Scientific Reports*, *7*(1), 8170. https://doi.org/10.1038/s41598-017-08467-z

Kosty, J. A., Zhao, K. X., Stewart, A. L., McCoy, D. E., Bianchi, D., & Manucharyan, G. E. (2025). Marine mammal-based observations of subsurface-intensified eddies in the seasonally sea ice-covered southern ocean. *Journal of Geophysical Research: Oceans*, *130*(4), e2024JC021781. https://doi.org/10.1029/2024JC021781

Li, X., Wang, Q., Danilov, S., Koldunov, N., Liu, C., Müller, V., et al. (2024). Eddy activity in the Arctic Ocean projected to surge in a warming world. *Nature Climate Change*, *14*(2), 156–162. https://doi.org/10.1038/s41558-023-01908-w

Loose, B., Fer, I., Ulfsbo, A., Chierici, M., Droste, E. S., Nomura, D., et al. (2024). An analysis of air-sea gas exchange for the entire MOSAiC Arctic drift. *Elementa: Science of the Anthropocene*, *12*(1), 00128. https://doi.org/10.1525/elementa.2023.00128

Lo Piccolo, A., Horvat, C., & Fox-Kemper, B. (2024). Energetics and transfer of submesoscale brine-driven eddies at a sea ice edge. *Journal of Physical Oceanography*, *54*(7), 1489–1501. https://doi.org/10.1175/JPO-D-23-0147.1

Maalouly, M., Lapeyre, G., Cozian, B., Mompean, G., & Berti, S. (2023). Particle dispersion and clustering in surface ocean turbulence with ageostrophic dynamics. *Physics of Fluids*, *35*(12), 126601. https://doi.org/10.1063/5.0174665

Manley, T. O., & Hunkins, K. (1985). Mesoscale eddies of the Arctic Ocean. *Journal of Geophysical Research*, *90*(C3), 4911–4930. https://doi.org/10.1029/JC090iC03p04911

Manucharyan, G. E., Lopez-Acosta, R., & Wilhelmus, M. M. (2022). Spinning ice floes reveal intensification of mesoscale eddies in the western Arctic Ocean. *Scientific Reports*, *12*(1), 7070. https://doi.org/10.1038/s41598-022-10712-z

Manucharyan, G. E., & Thompson, A. F. (2017). Submesoscale Sea Ice-Ocean interactions in marginal Ice zones. *Journal of Geophysical Research: Oceans*, *122*(12), 9455–9475. https://doi.org/10.1002/2017JC012895

Manucharyan, G. E., & Thompson, A. F. (2022). Heavy footprints of upper-ocean eddies on weakened arctic sea ice in marginal ice zones. *Nature Communications*, *13*(1), 2147. https://doi.org/10.1038/s41467-022-29663-0

Marshall, J., Adcroft, A., Hill, C., Perelman, L., & Heisey, C. (1997). A finite-volume, incompressible Navier Stokes model for studies of the ocean on parallel computers. *Journal of Geophysical Research*, *102*(C3), 5753–5766. https://doi.org/10.1029/96JC02775

Marshall, J., Hill, C., Perelman, L., & Adcroft, A. (1997). Hydrostatic, quasi-hydrostatic, and non-hydrostatic ocean modelling. *Journal of Geophysical Research*. https://doi.org/10.1029/96JC02776

Martínez-Moreno, J., Lique, C., & Talandier, C. (2025). Sea ice heterogeneity as a result of ocean eddy activity during the ice growth season. *Geophysical Research Letters*, *52*(3), e2024GL113645. https://doi.org/10.1029/2024GL113645

Martinson, D. G., & McKee, D. C. (2012). Transport of warm upper circumpolar deep water onto the western Antarctic Peninsula continental shelf. *Ocean Science*, *8*(4), 433–442. https://doi.org/10.5194/os-8-433-2012

Mchedlishvili, A., Lüpkes, C., Petty, A., Tsamados, M., & Spreen, G. (2023). New estimates of Pan-Arctic sea ice–atmosphere neutral drag coefficients from ICESAT-2 elevation data. *The Cryosphere*, *17*(9), 4103–4131. https://doi.org/10.5194/tc-17-4103-2023

Meneghello, G., Marshall, J., Campin, J.-M., Doddridge, E., & Timmermans, M.-l. (2018). The ice-ocean governor: Ice-ocean stress feedback limits Beaufort Gyre Spin-Up. *Geophysical Research Letters*, *45*(20), 11293–11299. https://doi.org/10.1029/2018GL080171

Meneghello, G., Marshall, J., Lique, C., Isachsen, P. E., Doddridge, E., Campin, J.-M., et al. (2021). Genesis and decay of mesoscale baroclinic eddies in the seasonally ice-covered interior arctic ocean. *Journal of Physical Oceanography*, *51*(1), 115–129. https://doi.org/10.1175/JPO-D-20-0054.1

Mensa, J. A., & Timmermans, M.-L. (2017). Characterizing the seasonal cycle of upper-ocean flows under multi-year sea ice. *Ocean Modelling*, *113*, 115–130. https://doi.org/10.1016/j.ocemod.2017.03.009

Mokus, N. G. A., & Montiel, F. (2022). Wave-triggered breakup in the marginal ice zone generates lognormal floe size distributions: A simulation study. *The Cryosphere*, *16*(10), 4447–4472. https://doi.org/10.5194/tc-16-4447-2022

Moncada, R., Gupta, M., Thompson, A., & Andrade, J. E. (2023). Level set discrete element method for modeling sea ice floes. *Computer Methods in Applied Mechanics and Engineering*, *406*, 115891. https://doi.org/10.1016/j.cma.2023.115891

Moncada, R., Gupta, M., Thompson, A. F., & Andrade, J. E. (2025). Comparing the role of floe breakage and melt on summer sea ice loss. *Journal of Geophysical Research: Oceans*, *130*(4), e2024JC021223. https://doi.org/10.1029/2024JC021223

Muller, V., Wang, Q., Koldunov, N., Danilov, S., Sidorenko, D., & Jung, T. (2024). Variability of eddy kinetic energy in the Eurasian basin of the Arctic Ocean inferred from a model simulation at 1-km resolution. *Journal of Geophysical Research: Oceans*, *129*(3), e2023JC020139. https://doi.org/10.1029/2023JC020139

Nomura, D., Kawaguchi, Y., Webb, A. L., Li, Y., Dall'osto, M., Schmidt, K., et al. (2023). Meltwater layer dynamics in a central arctic lead: Effects of lead width, re-freezing, and mixing during late summer. *Elementa: Science of the Anthropocene*, *11*(1), 00102. https://doi.org/10.1525/elementa.2022.00102

Ou, H. W., & Gordon, A. L. (1986). Spin-down of baroclinic eddies under sea ice. *Journal of Geophysical Research*, *91*(C6), 7623–7630. https://doi.org/10.1029/jc091ic06p07623

Padman, L. (1995). Small-scale physical processes in the Arctic Ocean. In *Arctic oceanography: Marginal ice zones and continental shelves* (pp. 97–129). American Geophysical Union (AGU). https://doi.org/10.1029/CE049p0097

Perovich, D. K., Light, B., Eicken, H., Jones, K. F., Runciman, K., & Nghiem, S. V. (2007). Increasing solar heating of the Arctic Ocean and adjacent seas, 1979–2005: Attribution and role in the ice-albedo feedback. *Geophysical Research Letters*, *34*(19). https://doi.org/10.1029/2007GL031480

Planat, N., Dufour, C. O., Lique, C., Rieck, J. K., Talandier, C., & Tremblay, L. B. (2025). Characteristics of ocean mesoscale eddies in the Canadian basin from a high resolution Pan-Arctic model. *EGUsphere*, *2025*, 1–39. https://doi.org/10.5194/egusphere-2025-3527

Pnyushkov, A., Polyakov, I. V., Padman, L., & Nguyen, A. T. (2018). Structure and dynamics of mesoscale eddies over the Laptev Sea continental slope in the Arctic Ocean. *Ocean Science*, *14*(5), 1329–1347. https://doi.org/10.5194/os-14-1329-2018

Prend, C. J., Swart, S., Stewart, A. L., du Plessis, M. D., Manucharyan, G. E., & Thompson, A. F. (2025). Observed regimes of submesoscale dynamics in the Southern Ocean seasonal ice zone. *Nature Communications*, *16*(1), 8344. https://doi.org/10.1038/s41467-025-63775-7

Ramadhan, A., Wagner, G. L., Hill, C., Campin, J.-M., Churavy, V., Besard, T., et al. (2020). Oceananigans.jl: Fast and friendly geophysical fluid dynamics on GPUS. *Journal of Open Source Software*, *5*(53), 2018. https://doi.org/10.21105/joss.02018

Rampal, P., Weiss, J., Dubois, C., & Campin, J.-M. (2011). IPCC climate models do not capture arctic sea ice drift acceleration: Consequences in terms of projected sea ice thinning and decline. *Journal of Geophysical Research*, *116*(C8), C00D07. https://doi.org/10.1029/2011JC007110

Roach, L. A., Smith, M. M., Herman, A., & Ringeisen, D. (2024). Physics of the seasonal sea ice zone. *Annual Review of Marine Science*, *17*(1), 355–379. https://doi.org/10.1146/annurev-marine-121422-015323

Rolph, R. J., Feltham, D. L., & Schröder, D. (2020). Changes of the arctic marginal ice zone during the satellite era. *The Cryosphere*, *14*(6), 1971–1984. https://doi.org/10.5194/tc-14-1971-2020

Shrestha, K., & Manucharyan, G. E. (2022). Parameterization of submesoscale mixed layer restratification under sea ice. *Journal of Physical Oceanography*, *52*(3), 419–435. https://doi.org/10.1175/JPO-D-21-0024.1

Silvestri, S., Wagner, G. L., Campin, J.-M., Constantinou, N. C., Hill, C. N., Souza, A., & Ferrari, R. (2024). A new WENO-based momentum advection scheme for simulations of ocean mesoscale turbulence. *Journal of Advances in Modeling Earth Systems*, *16*(7), e2023MS004130. https://doi.org/10.1029/2023MS004130

Silvestri, S., Wagner, G. L., Constantinou, N. C., Hill, C. N., Campin, J.-M., Souza, A. N., et al. (2025). A GPU-based ocean dynamical core for routine mesoscale-resolving climate simulations. *Journal of Advances in Modeling Earth Systems*, *17*(4), e2024MS004465. https://doi.org/10.1029/2024MS004465

Smith, M. M., Angot, H., Chamberlain, E. J., Droste, E. S., Karam, S., Muilwijk, M., et al. (2023). Thin and transient meltwater layers and false bottoms in the arctic sea ice pack—recent insights on these historically overlooked features. *Elementa: Science of the Anthropocene*, *11*(1), 00025. https://doi.org/10.1525/elementa.2023.00025

Smith, M. M., Fuchs, N., Salganik, E., Perovich, D. K., Raphael, I., Granskog, M. A., et al. (2025). Formation and fate of freshwater on an ice floe in the central Arctic. *The Cryosphere*, *19*(2), 619–644. https://doi.org/10.5194/tc-19-619-2025

Stephens, B. B., & Keeling, R. F. (2000). The influence of Antarctic sea ice on glacial–interglacial CO2 variations. *Nature*, *404*(6774), 171–174. https://doi.org/10.1038/35004556

Stern, H. L., Schweiger, A. J., Zhang, J., & Steele, M. (2018). On reconciling disparate studies of the sea-ice floe size distribution. *Elementa: Science of the Anthropocene*, *6*, 49. https://doi.org/10.1525/elementa.304

Sumata, H., de Steur, L., Divine, D. V., Granskog, M. A., & Gerland, S. (2023). Regime shift in Arctic Ocean sea ice thickness. *Nature*, *615*(7952), 443–449. https://doi.org/10.1038/s41586-022-05686-x

Swart, S., du Plessis, M. D., Thompson, A. F., Biddle, L. C., Giddy, I., Linders, T., et al. (2020). Submesoscale fronts in the Antarctic marginal ice zone and their response to wind forcing. *Geophysical Research Letters*, *47*(6), e2019GL086649. https://doi.org/10.1029/2019GL086649

Thomson, J. (2022). Wave propagation in the marginal ice zone: Connections and feedback mechanisms within the air–ice–ocean system. *Philosophical Transactions of the Royal Society A: Mathematical, Physical and Engineering Sciences*, *380*(2235), 20210251. https://doi.org/10.1098/rsta.2021.0251

Thorndike, A. S. (1992). A toy model linking atmospheric thermal radiation and sea ice growth. *Journal of Geophysical Research*, *97*(C6), 9401–9410. https://doi.org/10.1029/92JC00695

Timmermans, M.-L., Toole, J., & Krishfield, R. (2018). Warming of the interior Arctic Ocean linked to sea ice losses at the basin margins. *Science Advances*, *4*(8), eaat6773. https://doi.org/10.1126/sciadv.aat6773

Toyota, T., Takatsuji, S., & Nakayama, M. (2006). Characteristics of sea ice floe size distribution in the seasonal ice zone. *Geophysical Research Letters*, *33*(2). https://doi.org/10.1029/2005GL024556

Vichi, M. (2022). An indicator of sea ice variability for the Antarctic marginal ice zone. *The Cryosphere*, *16*(10), 4087–4106. https://doi.org/10.5194/tc-16-4087-2022

West, B., O'Connor, D., Parno, M., Krackow, M., & Polashenski, C. (2022). Bonded discrete element simulations of sea ice with non-local failure: Applications to nares strait. *Journal of Advances in Modeling Earth Systems*, *14*(6), e2021MS002614. https://doi.org/10.1029/2021MS002614

Wilchinsky, A. V., & Feltham, D. L. (2006). Modelling the rheology of sea ice as a collection of diamond-shaped floes. *Journal of Non-Newtonian Fluid Mechanics*, *138*(1), 22–32. https://doi.org/10.1016/j.jnnfm.2006.05.001

Zhang, J., Weijer, W., Steele, M., Cheng, W., Verma, T., & Veneziani, M. (2021). Labrador Sea freshening linked to Beaufort Gyre freshwater release. *Nature Communications*, *12*(1), 1229. https://doi.org/10.1038/s41467-021-21470-3

Zhang, Xue, H., Chai, F., & Ni, Q. (2015). Dynamical processes within an anticyclonic eddy revealed from Argo floats. *Geophysical Research Letters*, *42*(7), 2342–2350. https://doi.org/10.1002/2015GL063120

Zhao, M., Timmermans, M.-L., Cole, S., Krishfield, R., Proshutinsky, A., & Toole, J. (2014). Characterizing the eddy field in the Arctic Ocean halocline. *Journal of Geophysical Research: Oceans*, *119*(12), 8800–8817. https://doi.org/10.1002/2014JC010488

Zhou, S., Meijers, A. J. S., Meredith, M. P., Abrahamsen, E. P., Holland, P. R., Silvano, A., et al. (2023). Slowdown of Antarctic Bottom Water export driven by climatic wind and sea-ice changes. *Nature Climate Change*, *13*(7), 701–709. https://doi.org/10.1038/s41558-023-01695-4